Supplemental Data

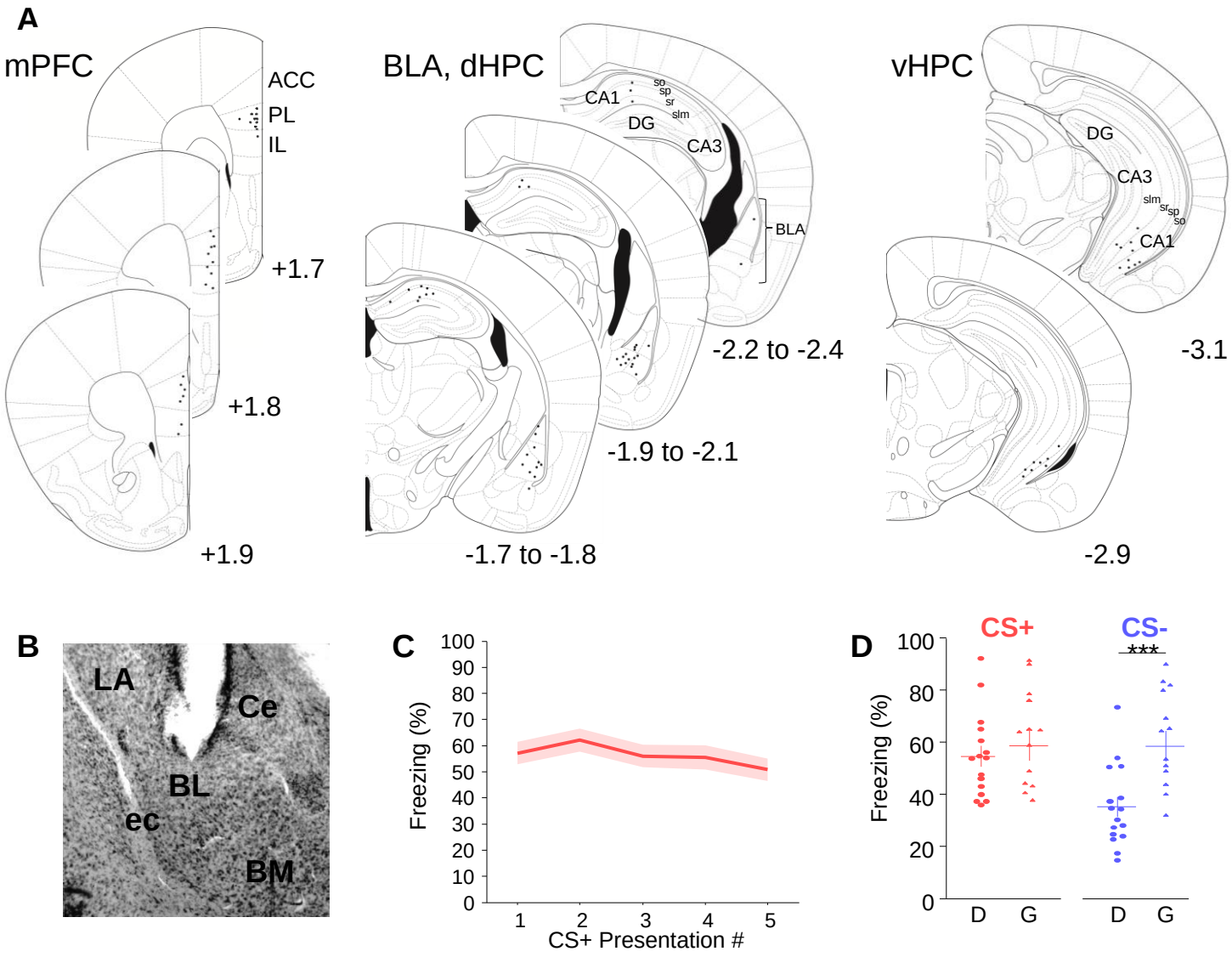

Figure S1, associated with Figure 1. BLA-mPFC-vHPC recordings during fear and safety.

(A) Location of electrolytic lesions from electrodes included in this study for the mPFC (left), BLA(middle), dHPC (middle), and vHPC (right). Lesion locations are indicated by a black dot. Numbers indicate AP level relative to bregma. ACC, anterior cingulate cortex; PL, prelimbic cortex; IL, infralimbic cortex; DG, dentate gyrus; so, stratum oriens; sp, stratum pyramidale; sr, stratum radiatum; slm, stratum lacunosum moleculare. Figure adapted from Franklin-Paxinos Atlas.

(B) Representative histology after an electrolytic lesion from a BLA stereotrode bundle. LA, lateral nucleus; BL, basolateral nuclei; BM, basomedial nuclei; Ce, central nucleus; ec, external capsule.

(C) Average freezing rate (+/- SEM) during CS+ tone presentations as a function of recall trial number.

(D) Freezing rates of discriminators (D, circles) and generalizers (G, triangles) during CS+ (red) and CS- (blue) presentations, averaged across five trials. *** $p < .001$, sign-rank test.

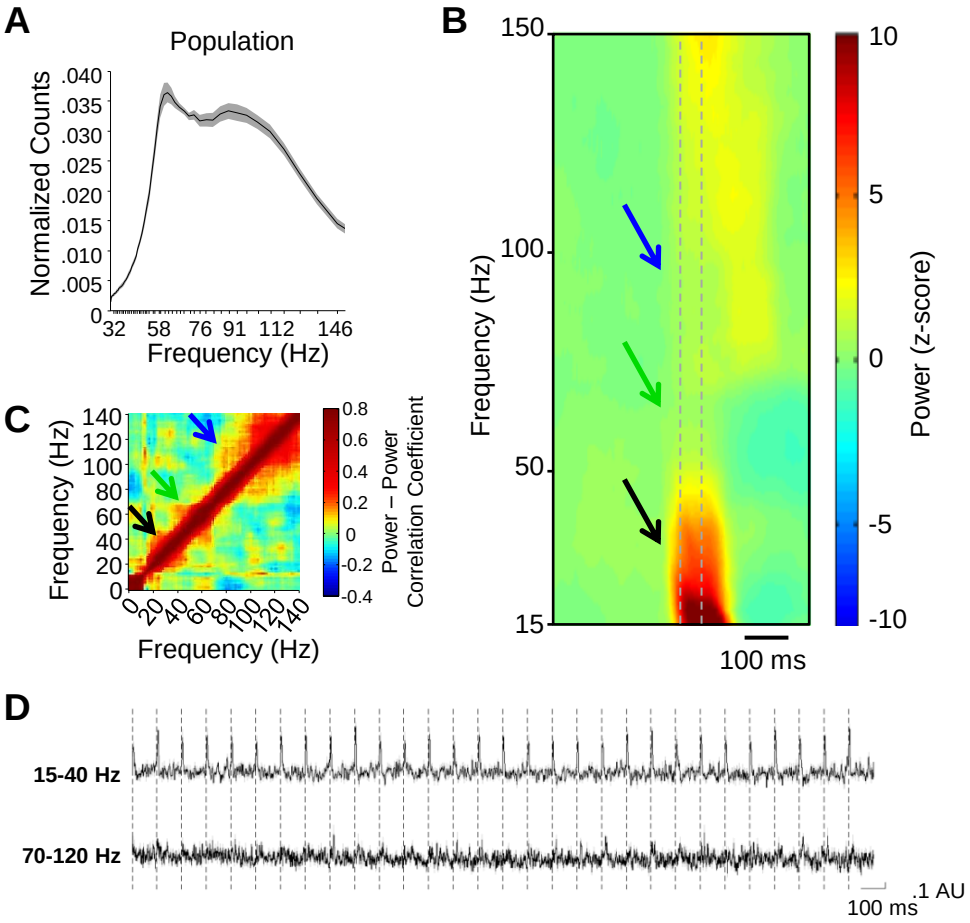

Figure S2, associated with Figure 1. Three bands of high frequency activity in the BLA.

(A) Instantaneous gamma frequency (see Supplementary Experimental Procedures) was calculated for activity between 30 and 150 Hz. The probability of observing each instantaneous frequency is plotted. The x-axis is scaled to reflect that frequency was calculated from the reciprocal of the peak-to-trough and trough-to-peak distances.

(B) CS+ pip-triggered multitaper power, averaged across trials for all animals. Stippled gray lines indicate pip onset and offset. Power was separately z-scored in each frequency band. Blue arrow, fast gamma band (70-120 Hz); green arrow, slow gamma band (40-70 Hz); black arrow, pip-evoked band (15-40 Hz)

(C) Power-power comodugram plotting the strength of power co-modulation between different frequency bands. Each pixel indicates the Pearson's correlation coefficient for multitaper power between two different frequencies for a single animal.

(D) LFP activity filtered for pip-evoked or fast gamma band for a single animal during CS+ presentations, averaged across 5 trials. Stippled black lines indicate times of pip onset.

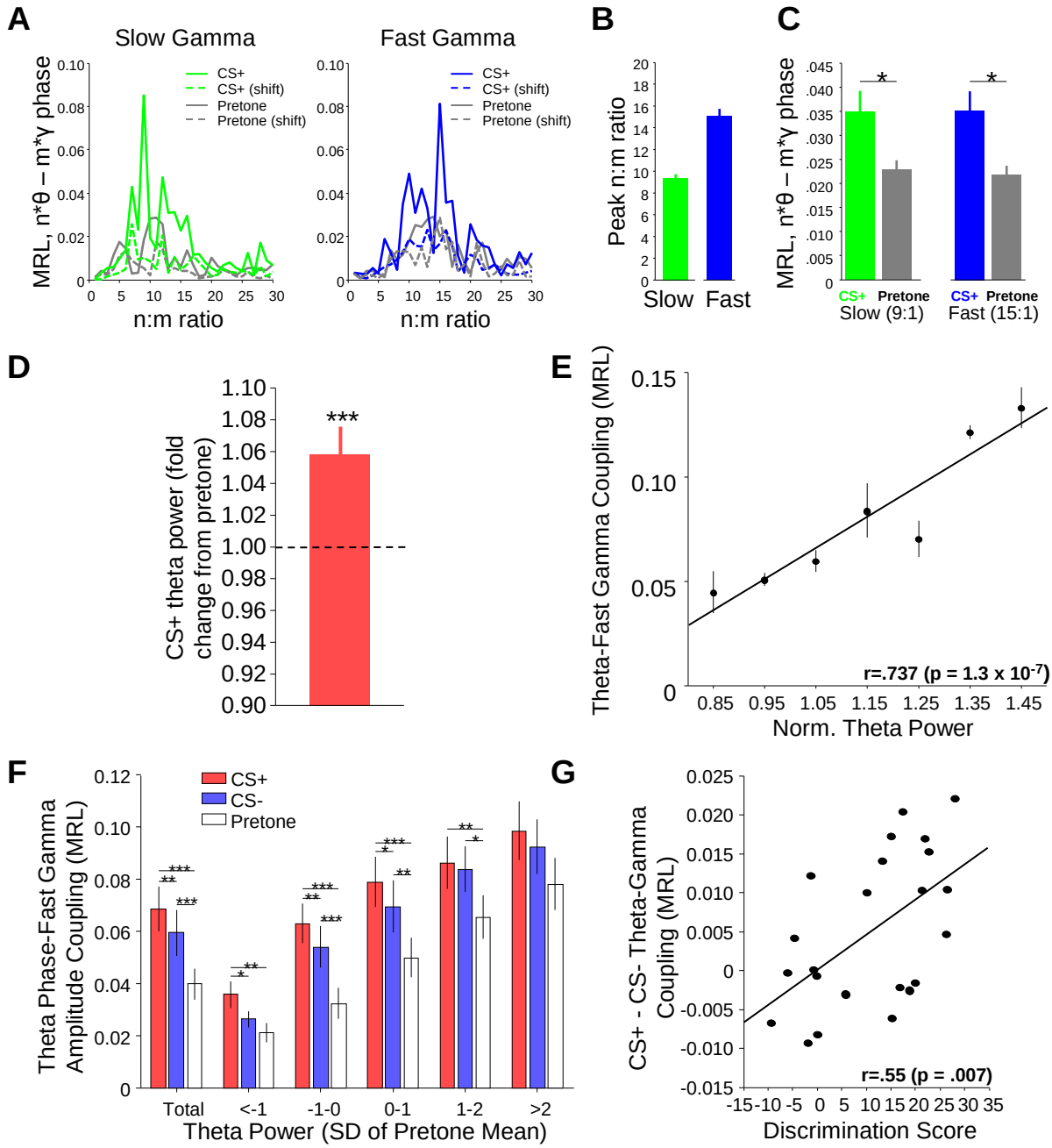

Figure S3, associated with Figure 2. Theta-gamma coupling is enhanced by fear.

(A) MRL values for n*theta phase – m*gamma phase distribution for a single animal for phases filtered in the slow gamma (left, green) and fast gamma (right, blue) range in the CS+ (blue/green) and pretone (gray) along with shift predictors.

(B) The n:m ratio at the peak MRL value for slow (green) and fast gamma (blue) with theta, averaged across animals.

(C) Average MRL values for phase-phase coupling of slow (green, 9:1) and fast gamma (blue, 15:1) during CS+ and pretone.

(D) Average fold change in theta power during CS+ presentations compared to pretone. *** p < .001, sign-rank (to test median of 1).

(E) Average theta–fast gamma coupling as a function of theta power with multiple linear regression. Error bars indicate SEM.

(F) Theta-fast gamma coupling strength in the CS+ (red), CS- (blue), and pretone (white), in different bands of power (defined as standard deviations of pretone mean)

(G) Change in theta-gamma coupling strength from CS- to CS+ as a function of discrimination score.

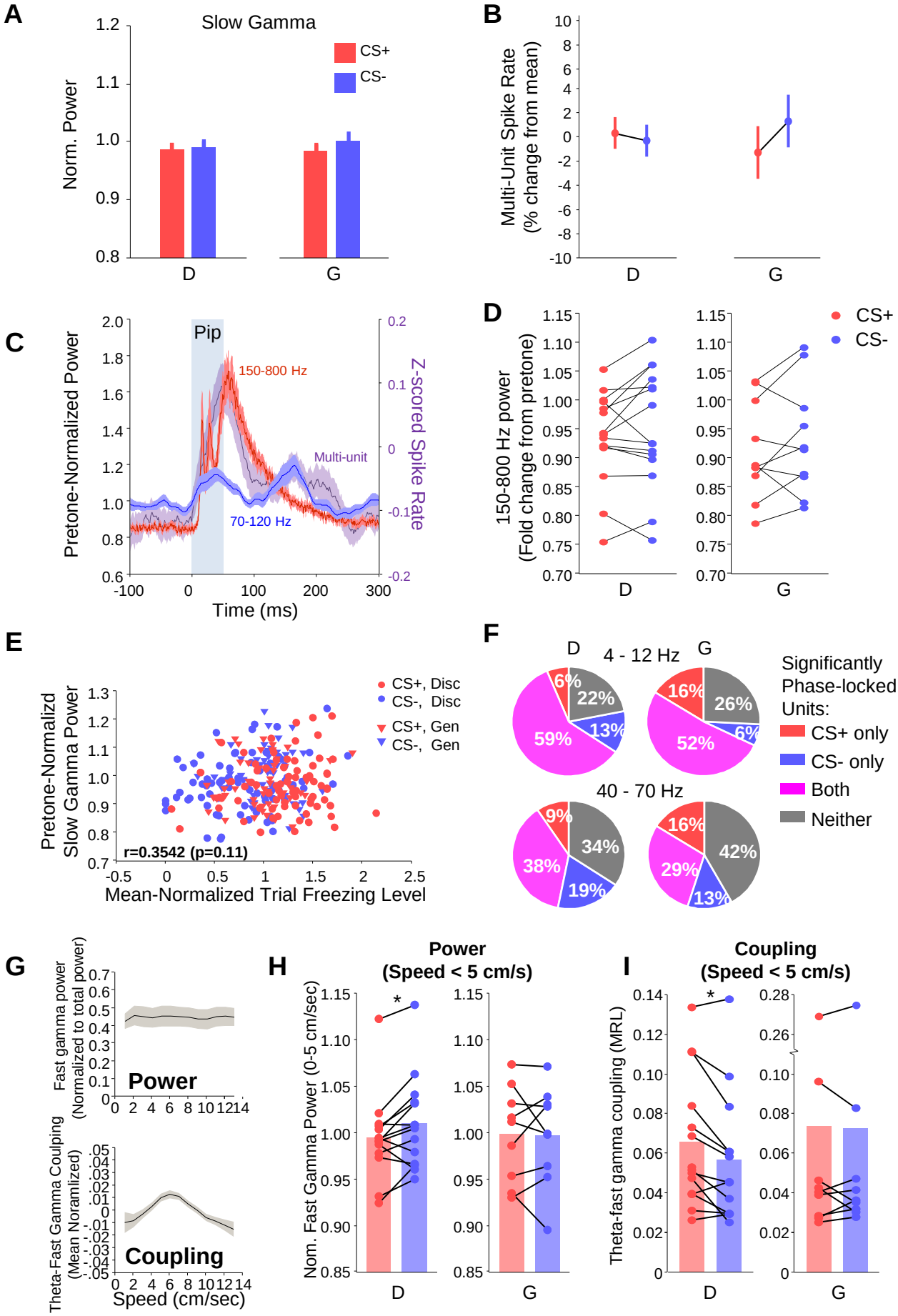
A
Slow Gamma
CS+
CS-
Norm. Power
D
G
B
Multi-Unit Spike Rate
(% change from mean)
C
Pip
150-800 Hz
Multi-unit
70-120 Hz
Pretone-Normalized Power
Z-scored Spike Rate
Time (ms)
D
150-800 Hz power
(Fold change from pretone)
E
Pretone-Normalizd
Slow Gamma Power
CS+, Disc
CS-, Disc
CS+, Gen
CS-, Gen
r=0.3542 (p=0.11)
Mean-Normalized Trial Freezing Level
F
4 - 12 Hz
40 - 70 Hz
Significantly
Phase-locked
Units:
CS+ only
CS- only
Both
Neither
G
Fast gamma power
(Normalized to total power)
Power
Theta-Fast Gamma Coulping
(Mean Noramlized)
Coupling
Speed (cm/sec)
H
Power
(Speed < 5 cm/s)
Nom. Fast Gamma Power (0-5 cm/sec)
I
Coupling
(Speed < 5 cm/s)
Theta-fast gamma coupling (MRL)

Figure S4, associated with Figure 3. Safety-related changes are specific to the fast gamma band and not due to changes in locomotion.

(A) Slow gamma power during CS+ (red) and CS- (blue) for discriminators (D) and generalizers (G).
(B) Multi-unit spike rate in discriminators (left) and generalizers (right) during the CS+ (red) and CS- (blue).
(C) Pip-evoked power in the 150-800 Hz range (red) and 70-120 Hz range (blue), with superimposed z-scored multi-unit spike rate (violet). The grey box indicates the time of the pip.
(D) 150-800 Hz power during the CS+ (red) and CS- (blue) for individual discriminators (left) and generalizers (right). Black lines connect data from individual animals.
(E) Trial-by-trial slow gamma power plotted as a function of trial-by-trial freezing. Data is plotted for discriminators (circles) and generalizers (triangles) for both CS+ (red) and CS- (blue). No significant correlation was found (r and p, multiple linear regression).
(F) Pie charts plotting the percentage of units phase-locked during the CS+ (red), CS- (blue), or both (magenta) to theta oscillations (top) or slow gamma oscillations (bottom) in both discriminators (left) and generalizers (right).
(G) Fast gamma power (normalized to total power) and theta-fast gamma coupling as a function of moment-to-moment velocity (cm/s).
(H) Pre-tone normalized fast gamma power during the CS+ (red) and CS- (blue) for discriminators (left) and generalizers (right) for periods of time when speed was less than 5 cm/s (relative immobility). * $p < .05$, sign-rank test
(I) Theta-Fast gamma coupling strength (MRL) during the CS+ (red) and CS- (blue) for discriminators (D) and generalizers (G) for periods of time when speed was less than 5 cm/s (relative immobility). * $p < .05$, sign-rank test

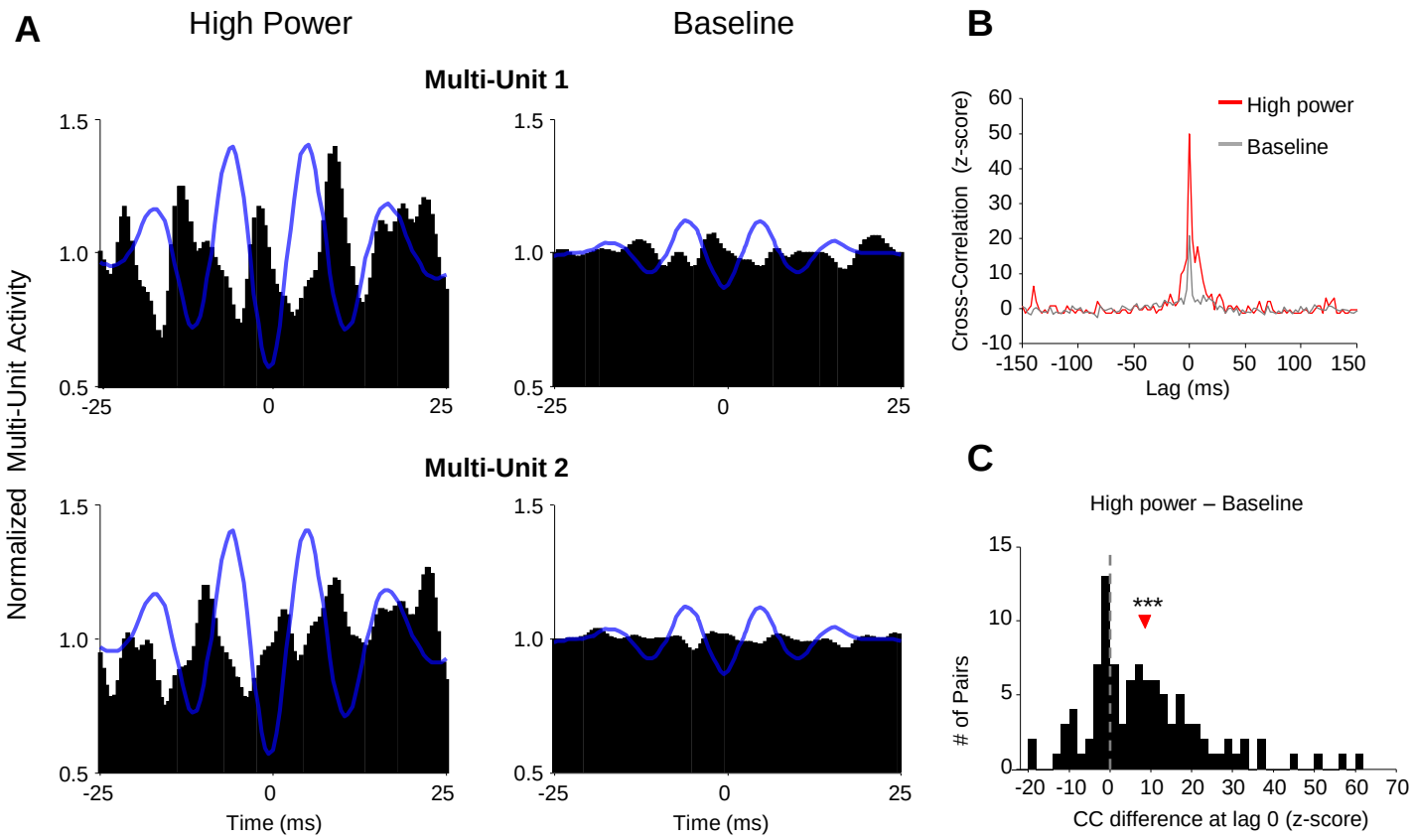

Figure S5, associated with Figure 4. BLA spiking is synchronized during fast gamma oscillations.

(A) Gamma trough-triggered histograms of spike counts from two representative multi-unit recordings, mean-normalized and separated for periods of elevated fast gamma power (>1.5 SD of pretone mean; left) vs baseline (<1.5 SD of pretone mean; right). Blue line, gamma trough-triggered LFP.

(B) Histogram quantifying the cross-correlation change from baseline to high power for all simultaneously recorded multi-unit pairs at lag 0. Triangle indicates median. *** Difference from 0, $p < .001$, sign-rank.

(C) Example cross-correlogram for the same units as in (B) during high power (red) and baseline (gray).

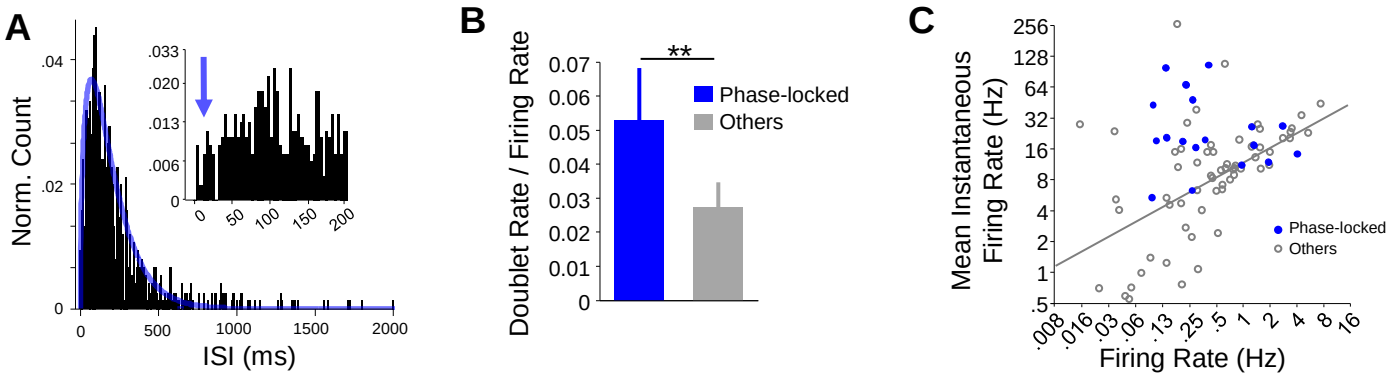

Figure S6, associated with Figure 5. Fast gamma phase-locked cells fire in doublets.

(A) Inter-spike interval histogram for the same unit as in (A). Blue line, gamma fit for Poisson distributed data. Inset, expanded time scale. Blue arrow indicates ISIs corresponding to doublet firing.

(B) The number of doublets (defined by ISI ≤ 40 ms) for phase-locked (blue) and other units (gray), normalized by firing rate. ** $p < .01$, sign-rank.

(C) Mean instantaneous firing rate (mean of 1/ISI) vs. overall mean firing rate. Phase-locked units are plotted in blue and others are plotted in gray. Gray line indicates the linear regression line for the non-phase locked cells.

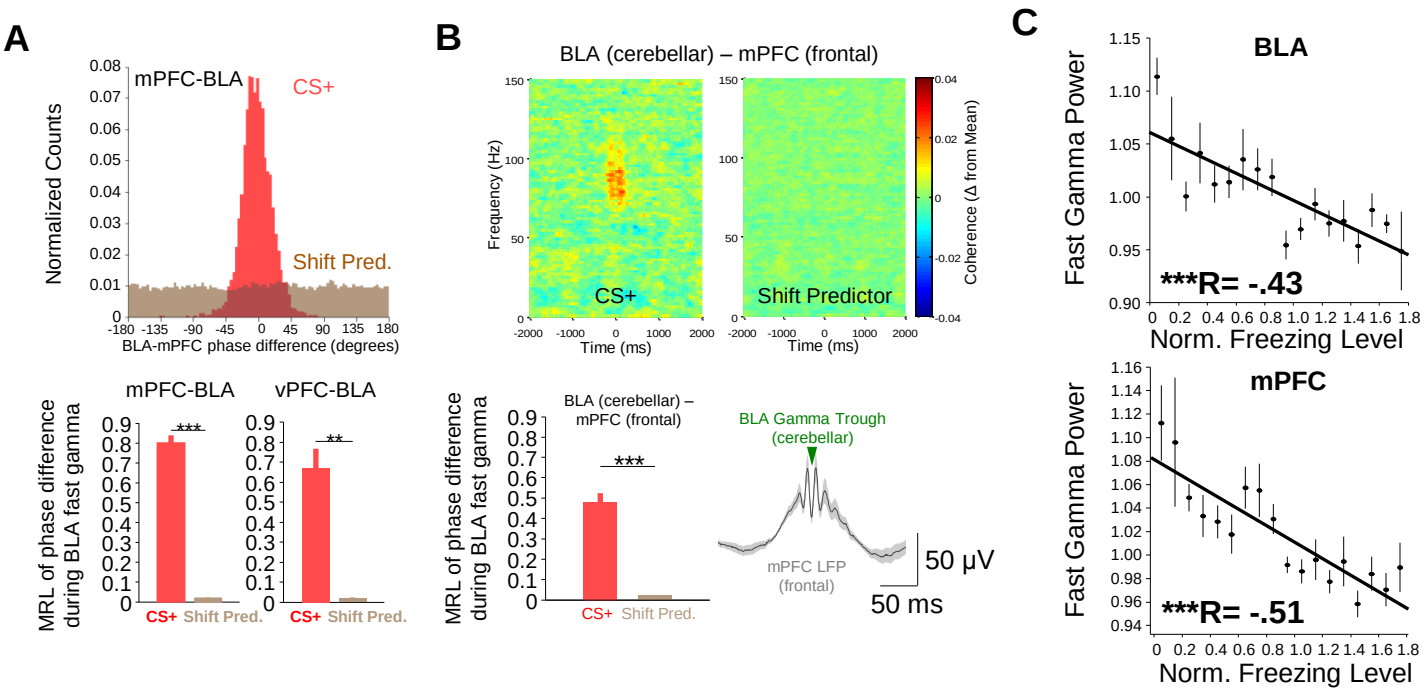

Figure S7, associated with Figure 6. Fast gamma oscillations synchronize the mPFC-BLA-vHPC network.

(A) Top, distribution of fast gamma mPFC-BLA phase-phase differences during BLA fast gamma oscillations in the CS+ (red) compared to shift predictor (brown) for a single animal. Bottom, average strength of unimodality of mPFC-BLA (left) and vHPC-BLA (right) phase-phase differences in the CS+ (red) compared to shift predictor (brown). *** p < .001, sign-rank; ** p < .01, sign-rank

(B) Top, BLA gamma-trough triggered mPFC-BLA spectral coherence during the CS+ (left) and shift predictor (right) for recordings referenced to different skull screws. BLA was referenced to the cerebellar screw and mPFC was referenced to the frontal screw. Bottom-left, average strength of unimodality of mPFC-BLA phase-phase differences in the CS+ (red) compared to shift predictor (brown), referenced as above. *** p < .001, sign-rank. Bottom-right, BLA (cerebellar reference) gamma trough-triggered mPFC (frontal reference) local field potential activity.

(C) Correlation between fast gamma power in the BLA (top) and mPFC (bottom) as a function of mean-normalized freezing level.

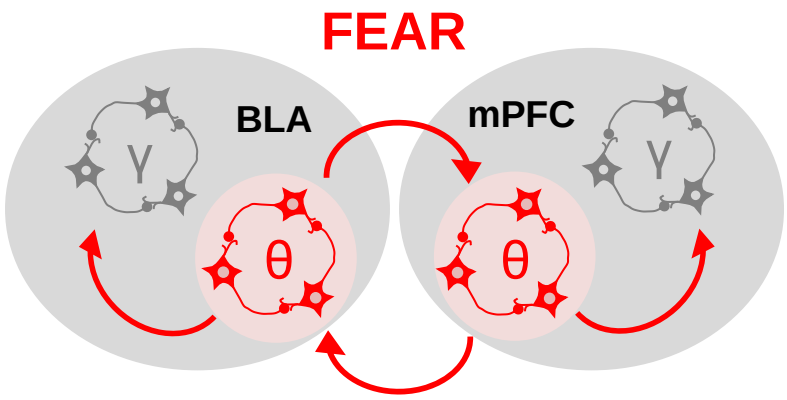

- **Decreased γ power**
- **Enhanced BLA θ-BLA γ coupling**

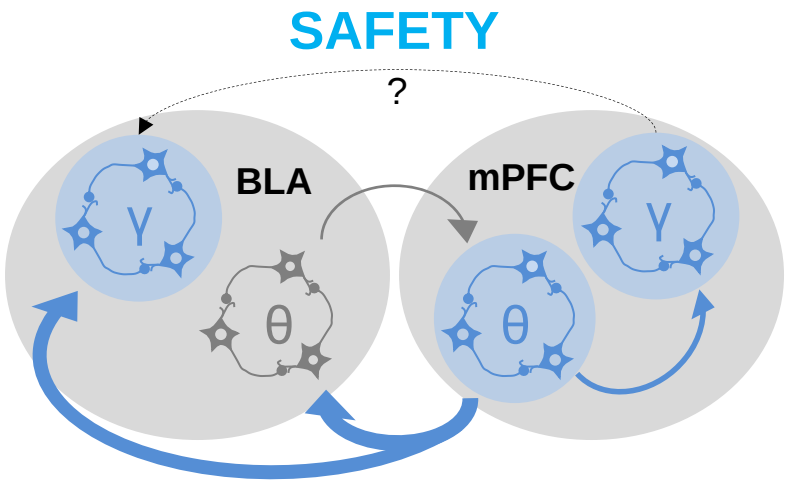

- **Increased γ power**
- **Enhanced mPFC→BLA directionality**
- **Enhanced PFC θ-BLA γ coupling**

Figure S8, associated with Figure 8. Different patterns of theta and gamma synchrony between the BLA and mPFC are observed during fear and safety.
This figure represents a hypothesized conceptual model. During fear, the BLA and mPFC are strongly synchronized in the theta range with bidirectional information transfer (Likhtik et al., 2014). This state is also characterized by enhancements in BLA theta-gamma coupling and a drop in gamma power in both the BLA and mPFC. During safety, synchrony is predominantly in the mPFC to BLA directional in both the theta (Likhtik et al., 2014) and gamma ranges (data from this study). This is associated with an enhancement of gamma power in both structures and coupling of BLA gamma to mPFC theta oscillations.

Supplemental Experimental Procedures

Animal housing

Mice were group housed on a 12-h light/dark cycle, until they were removed for surgery and moved to individual housing with enrichment (bedding squares). After surgery, mice were given analgesics (Carpofen, 5 mg/kg) and monitored throughout three days of recovery.

Electrophysiology

Single and multi-unit activity was recorded using five stereotrodes per animal. These stereotrodes were advanceable via a screw-based microdrive, while LFP wires were fixed in place. Stereotrode wires were never advanced within a recording day but were advanced between days. Stereotrodes were advanced by 80 microns after open field testing and by another 80 microns after fear recall testing. Single units were distinguished from multi-units if they were well clustered, as indicated by signal-to-noise ratio ≥ 3 and an solation distance ≥ 10 using an 8-dimensional feature space. Other recorded spikes above threshold (30-40 μV) were grouped together as multi-unit recordings. Multi-units contaminated with high frequency noise were excluded.

Histology

At the end of all experiments, animals were deeply anesthetized with ketamine (180 mg/kg). Current (50 μA, 10 s) was passed through each LFP electrode and one stereotrode in the stereotrode bundle to create lesions for target verification (Figure S1). Animals were then intra-cardially perfused and post-fixed for 3-7 days with 4% paraformaldehyde in phosphate-buffered saline. Tissue was subsequently cryo-protected in 30% sucrose in phosphate-buffered saline overnight. Brains were sectioned on a cryostat into 60 μm slices, mounted onto glass slides, and Nissl stained with cresyl violet. Only animals with proper electrode placement were included in the analysis (see Figure S1). Most mPFC placements (26/27) were localized to layer II/III, the output layer to the amygdala (McDonald, 1998), while most ventral and dorsal CA1 placements were in either stratum pyramidale or radiatum (Figure S1A).

LFP Power and Phase Analysis

To analyze LFP changes in multiple frequency domains, multi-taper spectrograms were calculated with a time window of 256 samples, 1024 FFTs, and a time-bandwidth product (NW) of 1.5 (2 tapers) using scripts provided by K. Harris and the Chronux Package (http://chronux.org; Mitra and Bokil, 2008). These parameters were chosen to provide good temporal resolution, but they do not offer suitable frequency resolution for activity in the theta range. Thus, power spectra were instead generated with 2048 samples, 1024 FFTs, and a time-bandwidth product of 1.5, averaging across time windows. The Morlet wavelet transform (q=3, for frequencies between 1 and 150 Hz) was used to investigate how power and phase changed together dynamically across time. In particular, we were able to observe switches between periods of slow gamma oscillations and fast gamma oscillations as in Figure 1B.

Only in a few recordings was a 60 Hz noise peak observable in the power spectrum. 60 Hz noise and its harmonics were removed with a least squares regression in the frequency domain (rmlinesmovingwinc, Chronux) using 800 ms windows, stepping by 200 ms. The 60 Hz noise was episodic and did not show any observable relationship to tone presentation or behavior of the animal. Thus, we were able to replicate all main results of the paper without noise removal.

To calculate the power envelope and phase of ongoing theta and gamma oscillations, a bandpass filter was applied using a zero-phase-delay FIR filter with Hamming window (filter0, provided by K. Harris and G. Buzsaki, New York University, USA) and the Hilbert transform of the bandpass-filtered signal was calculated. Different filter orders were used for different ranges to avoid inducing ringing artifacts: 1894 was used for theta (4-12 Hz), 400 was used for slow gamma (40-70 Hz), and 240 was used for fast gamma (70-120 Hz) and higher spectral power (150-800 Hz). These parameters were used throughout, unless otherwise noted. Results were not sensitive to the precise filter orders used, as sizes +/- 50% yielded similar results.

Due to potential asymmetries in the theta oscillations, we compared the results that we obtained from the Hilbert transform to phase values obtained by interpolation from troughs, peaks, and zero-crossings as in Belluscio et al. (2013). Likely due to less asymmetry in the BLA theta oscillation, these phase values would only infrequently deviate from those obtained from the Hilbert transform. Most analyses in the paper were repeated using both methods with no substantial differences obtained (data not shown), so the Hilbert transform was favored for computational efficiency and to be consistent with previous work (Adhikari et al., 2010, 2011; Likhtik et al., 2013; Sigurdsson et al., 2010). To normalize electrodes across sites and animals, power was calculated throughout as the fold change from pretone (30s before each tone on recall day, for a total of 5 minutes of data).

For gamma trough-triggered analyses, the troughs of gamma oscillations were identified as elevations of the power envelope in the 40-70 Hz or 70-120 Hz bandpass signal above 1.5 SDs of the pretone mean (typically corresponding to the top 7-8% of the data) and the trough was identified as a local minimum in the signal. Nearly identical results were obtained with peak-triggered averages. Activity around these troughs was then averaged to produce peri-event time histograms.

Theta-Gamma Coupling Analysis

To investigate the relationship between low frequency and high frequency oscillations (Figure 1C), frequency-frequency comodugrams were generated in a way similar to previously published methods (Colgin et al., 2009; Tort et al., 2010; Tort et al., 2009; Tort et al., 2008). Bands of low frequency activity were extracted with a bandpass width of 2 Hz (centers at 1 to 30 Hz) and tested for phase-amplitude coupling with multi-taper power between 30-150 Hz. This coupling was quantified by the mean resultant length (MRL), yielding a value between 0 (no coupling) and 1 (perfect coupling). The mean resultant length (MRL) was chosen because of the observed unimodal relationship of theta phase-gamma amplitude coupling in both the slow and fast gamma ranges and its higher statistical power compared to the non-parametric modulation index (Tort et al., 2010). We binned multitaper power into phase bins of width $\pi/9$ radians, corresponding to the contemporaneous theta phase. The resulting values were

input as weights for calculating the MRL (circ_r, circular statistics toolbox) with a correction for binned data (Berens, 2009). Binned data was utilized because of the sensitivity of the MRL statistic to sample size. We repeated this and subsequent analyses using the modulation index, which we calculated as previously described (Tort et al., 2010) with phase bins of width π/40 radians, in order to be sensitive to possible binomial distributions. The MRL and modulation index yielded the same pattern of results in all cases.

To investigate the relationship between theta phase and gamma power (Figure 2B, 7A), we generated theta phase-amplitude comodugrams as previously described (Belluscio et al., 2012). As described above, the mean multi-taper power was found for frequencies between 30 and 150 Hz (stepping by 2.5 ms) within phase bins of width π/40 radians. Power was normalized within each frequency range by z-scoring. Results from this analysis were compared to a shift predictor, obtained by shifting the gamma power signal relative to the theta phase by an integer number of seconds (1 to 29 seconds), and the results were averaged. This is also how shift prediction was performed for all other analyses.

For quantification of theta-gamma phase-amplitude coupling in the slow and fast gamma bands, we utilized the MRL for power envelope values binned into phase bins of width π/9 radians.

Instantaneous theta and gamma frequency was calculated from peaks and troughs identified using a custom algorithm. Instantaneous frequency was taken as the reciprocal of twice the peak-to-trough or trough-to-peak time. For analysis of theta-gamma coupling by instantaneous theta frequency (Figure 2D & E), data were binned into 1 Hz bins and the MRL was calculated for each bin. If any bin contained less than 5 seconds of data, the results for that analysis were excluded due to overestimation of coupling values for small sample sizes (Dvorak and Fenton, 2014).

Power-power comodugrams (Figure S2C) were generated as previously described (Buzsaki et al., 2003) using scripts provided by K. Harris. In brief, multi-taper power was calculated in non-overlapping time windows with the same parameters as above. The Pearson's correlation coefficient was calculated for power in each frequency compared to the power in every other frequency range across time windows to quantify power-power correlation strength.

Phase-phase coupling was assessed as previously described (Belluscio et al., 2012). In brief, n:m coupling patterns were tested for by extracting Hilbert phase values in the theta range and either slow or fast gamma range. If there is a consistent n:m relationship, the difference between n*theta phase and m*gamma phase should yield a consistent value. By varying values of n, the strongest n:m relationship can be assessed with the MRL of the distribution. The n:m relationship with the maximum MRL was calculated for each animal. The average peak n:m values were slow and fast gamma (9:1 and 15:1, respectively) was then used for comparing CS+ and pretone phase-phase coupling strengths.

Speed-filtered Analyis

Animal movements were tracked in the open field by an LED mounted on the headstage. Instantaneous velocity was calculated from the change in x and y position at each time step (33 Hz sample rate). Multitaper power was calculated as above and

averaged from 70-120 Hz for the entire open field session to calculate fast gamma power. Velocity was calculated in each multitaper window by averaging instantaneous velocity values. For coupling analysis, the fast gamma power envelope was calculated for each sample (1893 Hz sample rate) and the velocity was calculated for each sample by smoothing with a 182 ms (6 samples at 33 Hz) boxcar filter. For fast gamma power vs. velocity and theta-fast gamma coupling vs. velocity plots, results were calculated for velocity bins with a size of 2 cm/sec, centered between 1 and 13 cm/sec (>13 cm/sec constituted a small amount of time for this data set).

Immobility speed-limited analysis was restricted to windows when velocity was less than 5 cm/sec, corresponding to relative immobility.

Analysis of multi-site recordings

Coherence between the BLA, mPFC, and vHPC was calculated using multitaper coherence with a 256 sample length window, 1.5 time-bandwidth product (NW), 2 tapers, and 1024 FFTs. BLA gamma-trough triggered coherograms were calculated for a 4 second window around gamma troughs during periods of relatively high gamma power (>1.5 SD above pretone mean).

Periods of near zero phase-lag gamma synchrony were define by (1) both BLA and mPFC gamma power was >1.5 SD over the mean, and (2) the phase difference less than 30 degrees for at least one full gamma cycle. Phase differences were calculated by estimated from Hilbert-extracted phases.

Granger causality analysis was performed using arfit toolbox for Matlab. The order was determined for each mPFC-BLA LFP pair by Schwarz's Bayesian Criterion between 2 and 120 samples (1-60 ms). The strength of mPFC granger lead was calculated as $GCI^{mPFC \rightarrow BLA}$ / ($GCI^{mPFC \rightarrow BLA}$ + $GCI^{BLA \rightarrow mPFC}$) for each animal.

For Figure 7F, to correct for differences in the variance of coupling strength, differences in coupling were normalized by z-scoring with respect to the SD of the BLA theta-BLA gamma coupling.

mPFC and BLA theta lead probabilities were determined by iteratively performing mPFC-BLA power-power correlations as previously described (Likhtik et al., 2013; Adhikari et al., 2010). In brief, the raw LFP was filtered for theta (4-12 Hz, 400 sample FIR filter) and the power envelope was extracted with the Hilbert transform. Cross-correlation lag analysis was performed with 1 second windows, stepping by 5 ms. Lead probability was determined as the percentage of time windows which demonstrated leads in each direction.

Single and Multi-Unit Analysis

For phase-locking analysis, to avoid spurious phase-locking due to spectral bleed of spike activity into the gamma range, LFPs were taken from a nearby but different stereotrode than that on which spikes were recorded. Phase-locking of BLA unit or multi-unit activity to ongoing oscillatory activity was assessed by assigning each spike to the Hilbert phase corresponding to the nearest simultaneously recorded local field potential sample. The significance of the phase-locking relationship was calculated using the Rayleigh test (significance was determined at $p<.05$, unless otherwise noted). We confirmed that potential asymmetries in the oscillation did not cause spurious coupling by utilizing a shift predictor (as above) in which the spikes were shifted relative

to the oscillation. This yielded significant phase-locking at a chance level (5%). None of the non-significant multi-units were significant with a non-parametric omnibus test (Hodge-Agnes), suggesting that we were not missing any non-unimodal phase-locking patterns by using the Rayleigh test; thus, we favored the parametric Rayleigh test for analysis.

Phase-locking was quantified by the MRL of the resulting phase distribution. Because the MRL statistic is sensitive to spike number, the number of spikes used for the analysis was fixed for calculation of multi-unit phase-locking strength by averaging the MRL value calculated for 150 randomly sub-sampled spikes, repeated 3000 times. Multi-units with less than 150 spikes were excluded from analysis.

Spike-spike cross-correlations were calculated for simultaneously recorded multi-unit activity as previously described (Dayan and Abbott, 2001; Headley and Weinberger, 2013) using custom written scripts. In brief, pairwise differences in spike times were calculated across all spikes and binned into 2.5 ms time bins. The cross-correlation was calculated for spikes falling within periods of elevated fast gamma power (>1.5 SDs above the pretone mean) versus baseline (<1.5 SDs above the pretone mean). Cross-correlations are normalized by the SD of values at lags of -30 to -50 and +30 to +50 ms, to account for baseline differences in spike number across pairs.

Doublet rate was quantified by finding the number of pairs of spikes that occurred within 40 ms of each other (Pape et al., 1998). Triplets and other longer trains of spikes were much less frequent than doublets and were not included in the count; their inclusion or exclusion did not affect the results, however. Mean instantaneous firing rate was quantified by averaging the reciprocals of each interspike interval for a single unit.

Open Field Analysis

Analyses were limited to the zones of center, transition, and periphery by finding times when the distance from the center was 0 to 14.29 cm, 14.29 to 16.97 cm, and 16.97 cm to 25 cm (0-80, 80-95, and 95-140 pixels), respectively. Gamma power envelope and theta phase values were extracted for times corresponding to the mouse being located in a single zone and then used to calculate average power and theta-gamma coupling strength. Power and coupling strength were normalized by the average values across zones.

Supplemental References

Berens, P. (2009). CircStat: A MATLAB Toolbox for Circular Statistics. Journal of Statistical Software *31*, 1-21.

Buzsaki, G., Buhl, D.L., Harris, K.D., Csicsvari, J., Czeh, B., and Morozov, A. (2003). Hippocampal network patterns of activity in the mouse. Neuroscience *116*, 201-211.

Dayan, P., and Abbott, L.F. (2001). Theoretical neuroscience : computational and mathematical modeling of neural systems (Cambridge, Mass.: Massachusetts Institute of Technology Press).

Dvorak, D. and Fenton, A.A. (2014) Toward a proper estimation of phase-amplitude coupling in neural oscillations. Journal of Neuroscience Methods *225*, 42-56.

McDonald, A.J. (1998). Cortical pathways to the mammalian amygdala. Prog Neurobiol *55*, 257-332.

Mitra, P., and Bokil, H. (2008) Observed brain dynamics (New York, NY: Oxford University Press).

Tort, A.B., Komorowski, R., Eichenbaum, H., and Kopell, N. (2010). Measuring phase-amplitude coupling between neuronal oscillations of different frequencies. J Neurophysiol *104*, 1195-1210.

Tort, A.B., Kramer, M.A., Thorn, C., Gibson, D.J., Kubota, Y., Graybiel, A.M., and Kopell, N.J. (2008). Dynamic cross-frequency couplings of local field potential oscillations in rat striatum and hippocampus during performance of a T-maze task. Proceedings of the National Academy of Sciences of the United States of America *105*, 20517-20522.